



Moment budget and seismic potential of the Xianshuihe-Xiaojiang fault system, southeastern Tibetan Plateau

Li Yfin^a, Gang Luo^{b,c,*}, Mfian Lfui^d

^a State Key Laboratory of Earthquake Dynamics, Institute of Geology, China Earthquake Administration, Beijing 100029, China

^b School of Geodesy and Geomatics, Wuhan University, 129 Luoyu Road, Wuhan 430079, China

^c Key Laboratory of Geospace Environment and Geodesy, Ministry of Education, Wuhan University, 129 Luoyu Road, Wuhan 430079, China

^d Department of Geological Sciences, University of Missouri, Columbia, MO, USA

ARTICLE INFO

Keywords:

Moment balance

Geodetic measurement

Seismic catalogs

Seismic hazards

The Xianshuihe-Xiaojiang fault system

ABSTRACT

The Xianshuihe-Xiaojiang fault system (XXFS) is an important boundary fault in the model of tectonic extrusion in the southeastern Tibetan Plateau. It is also seismically active, having produced seven $M \geq 7.5$ earthquakes since 1480 CE. We compiled an integrated earthquake catalog to estimate seismic moment release rates along the XXFS since 1480 CE, and compared them with moment accumulation estimated from the updated GPS data. Our results show moment deficits of $\sim 2.49 \times 10^{20}$ Nm for the northern (the Xianshuihe fault) and $\sim 1.28 \times 10^{20}$ Nm for the central (the Anninghe-Zemuhe-Daofangshan fault) parts of the XXFS, equivalent to the moment release of $M \sim 7.5$ and $M \sim 7.4$ events, respectively. The southern part (the Xiaojiang fault), on the other hand, has a moment surplus, suggesting a relatively low seismic potential. Analysis of moment budget on segments of the fault system indicates six sections of moment deficits along the XXFS, including the Luhuo segment, the Qianfeng-Kangding segment, the Moxi-Anninghe segment, the section connecting the Anninghe and Zemuhe faults, the northern Zemuhe segment and the connecting section between the Zemuhe and Xiaojiang faults. Each section of moment deficit could allow an $M \sim 6.5$ event, whereas the Qianfeng-Kangding segment has the potential for an $M \sim 7.4$ event. The Anninghe segment, where no $M \geq 6.5$ event has occurred since 1536 CE, also deserves attention.

1. Introduction

The ~1000-km-long Xianshuihe-Xiaojiang fault system (XXFS) is one of the most tectonically active fault zones in the southeastern Tibetan Plateau (Fig. 1; Aifan et al., 1984; Aifan et al., 1991; Tappin et al., 2001; Xu et al., 2003; Wen et al., 2008; Zhang, 2013). Historical and instrumental earthquake records show that more than forty-one major earthquakes ($M > 6.0$), including ten $M \geq 7.5$ earthquakes, have occurred along the XXFS since 1480 CE (Fig. 2; Table S1; Wen et al., 2008). Hence, careful assessment of seismic hazards along the XXFS is imperative.

A piece of useful information for hazard assessment is the moment deficit (or surplus) on a fault, derived from comparison between geodetic moment accumulation and seismic moment release (e.g., Refid, 1910; Meade and Hager, 2005; Wang et al., 2010; Mazzotti et al., 2011; Wang et al., 2011; D'Agostino, 2014; Paolano et al., 2018; Ojo et al., 2021). The steady-state long-term rate of moment accumulation (the

geodetic moment rate) can be derived from geodetic measurements, such as Global Positioning System (GPS) data, after corrected for the influence of co- and post-seismic deformation of previous large earthquakes. On the other hand, seismicity can be used to estimate moment release rate. If the seismic moment release was less than the moment accumulation (a moment deficit), the system has strain energy to produce future earthquakes.

Previous studies have applied this approach to the XXFS. For example, Wang et al. (2011) estimated the moment accumulation rate based on fault slip rates and locking depth from a GPS-constrained elastic block model, and then compared it to the moment release rate derived from earthquake catalogs. They found a moment surplus along the XXFS. Wang et al. (2010), using a small-scale block model, found a moment surplus on the northern segment of Xianshuihe (XSH) but a moment deficit on the southern segment. However, fault slip rates estimated by elastic block models, therefore the geodetic moment estimate, can be sensitive to the simplification of fault geometry, especially

* Corresponding author at: School of Geodesy and Geomatics, Wuhan University, 129 Luoyu Road, Wuhan 430079, China.

E-mail addresses: gangluo66@gmail.com, gluo@sgg.whu.edu.cn (G. Luo).

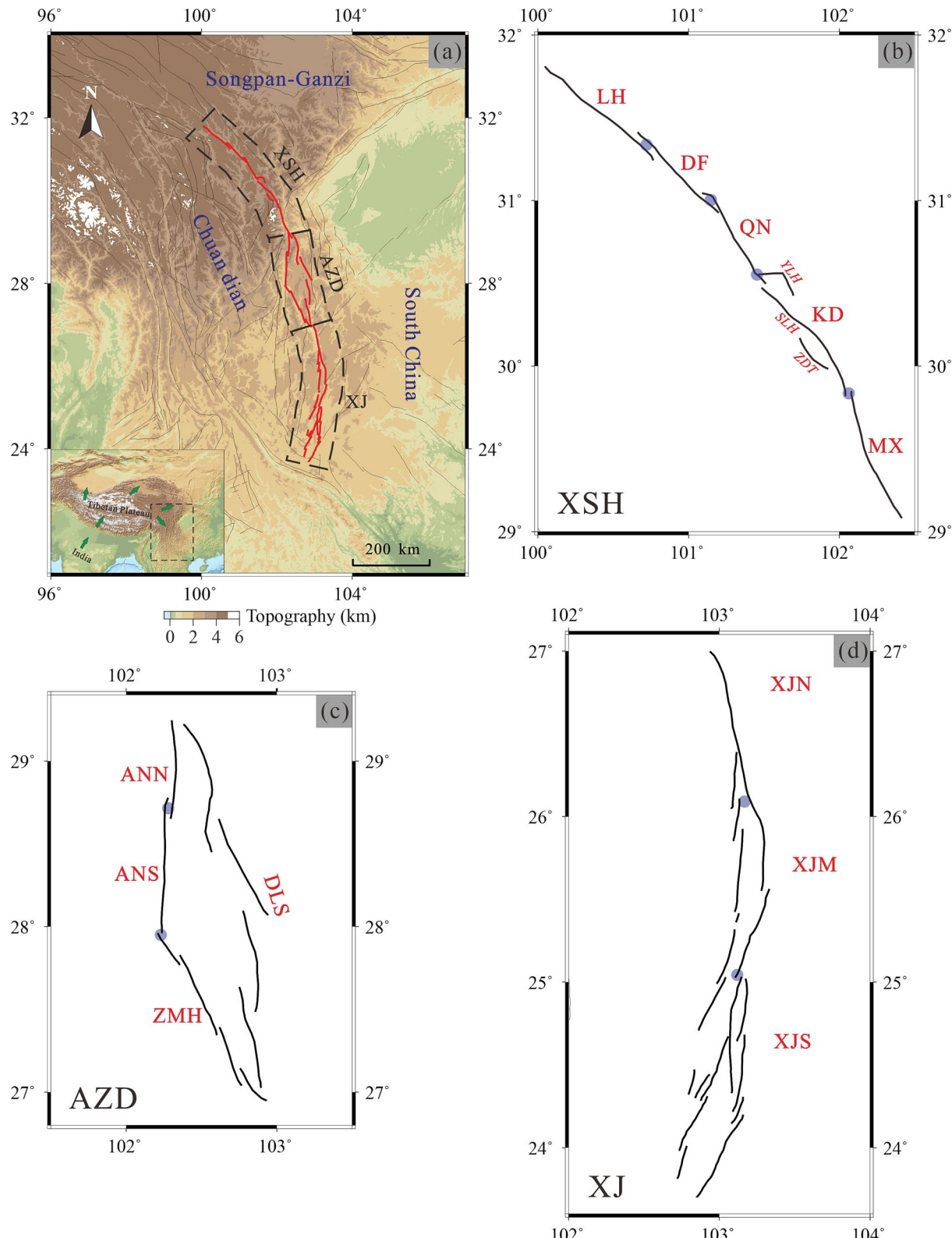


Fig. 1. (a) Tectonic map of the Xianshuhu-Xiaojiang fault system (XXFS). Black lines are faults; the red lines are main faults in the XXFS. The dashed polygonal regions indicate the seismic zones in which the seismic moment is calculated. The inset map shows the Tibetan Plateau. The dashed box in the inset map shows the location of the Chuandian region. Green arrows show the relative motion of the crust. (b-d) Black panels show fault traces of the XSH fault (b), the AZD fault (c), and the XJ fault (d). The blue dots are the endpoints of the fault segments used in the study, mainly based on fault geometry and discontinuity. Abbreviations: XSH, Xianshuhu seismic zone; AZD, Annfinghe-Zemuhe-Dafliangshan seismic zone; XJ, Xiaojiang seismic zone; LH, Luhuo segment; DF, Daofu segment; QN, Qianfeng segment; KD, Kangding segment; YLH, Yaflahe branch; SLH, Saflahe branch; Zhdutang branch; MX, Moxi segment; ANHN, north segment of Annfinghe fault; ANHS, south segment of Annfinghe fault; XJN, XJM and XJS are the northern, middle and southern segments of the XJ fault, respectively. (For interpretation of the references in this figure legend, the reader is referred to the web version of this article.)

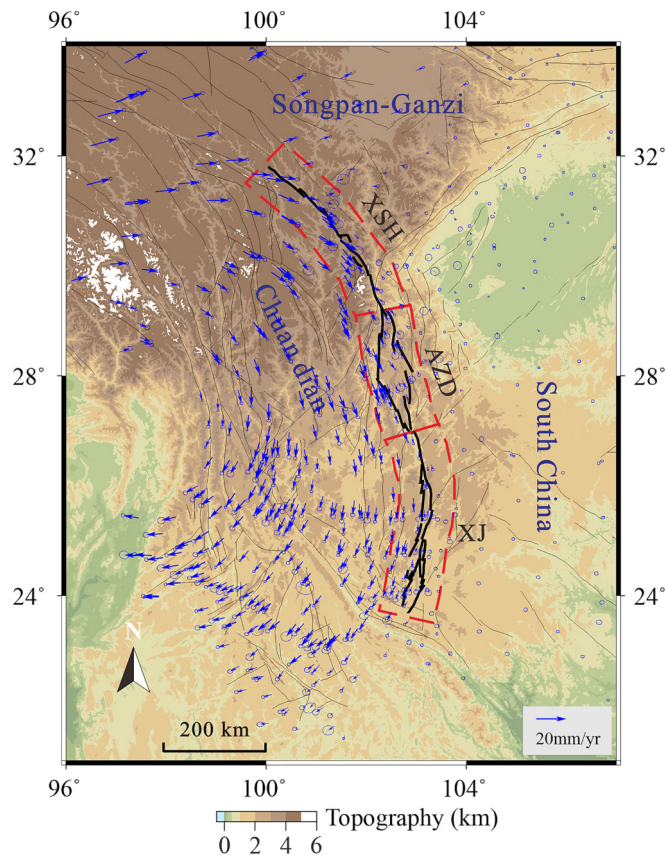


Fig. 2. Earthquakes in the Chuandian region. Yelllow cycles findicate historical earthquakes ($M \geq 4.0$). Blue cycles findicate instrumentally recorded earthquakes ($M \geq 4.0$). Data source: the National Earthquake Data Center of China (www.data.earthquake.cn). (For interpretation of the references to colour in this figure legend, the reader is referred to the web version of this article.)

large-scale models, and the simplification of fault zones to fault planes (e.g., Meade, 2002; Meade and Hager, 2005; Meade, 2007; Wang et al., 2010; Wang et al., 2011). Alternatively, others have divided the research fault zones into several closed regions, and calculated and compared the rates of geodetic moment accumulation with the moment release rate (e.g., Mazzotti et al., 2011; D'Agostino, 2014; Chou et al., 2015; Paolano et al., 2018; Sparacino et al., 2020; Ojo et al., 2021; Zhao et al., 2021). This approach can avoid the influence of simplified fault geometry and block division. For example, Zhao et al. (2021) calculated the moment budget of 14 seismic zones in the southeastern Tibetan Plateau and found that the moment accumulation in the XSH and Xiaojiaoliang (XJ) seismic zones has been largely released by earthquakes, while the Anninghe (ANH) seismic zone has a moment deficit. However, these studies have focused on the long-term moment budget of the entire seismic zone. Detailed analyses of the moment budget along the fault traces, which consist of many separated fault segments (Fig. 1), are needed to improve seismic hazard assessment of the XXFS.

The studies of moment budget and seismic potential require dense geodetic observation and long-term well-documented seismic catalogs. A rich seismic catalog including instrumentally recorded and historical earthquakes is available in the Sichuan-Yunnan (Chuandian) region of the southeastern Tibetan Plateau (Fig. 2). The Chuandian region also has a dense coverage of GPS station: 543 GPS stations and a high spatial density of $\sim 3.8 \times 10^4/\text{km}^2$ on average (Fig. 3; Wang and Shen, 2020). These earthquake and geodetic data allow a detailed analysis of moment budget along the XXFS.

In this study, we detailed a comparison of seismic moment release and geodetic moment accumulation along the XXFS, taking advantage of the updated GPS measurements in the southeastern

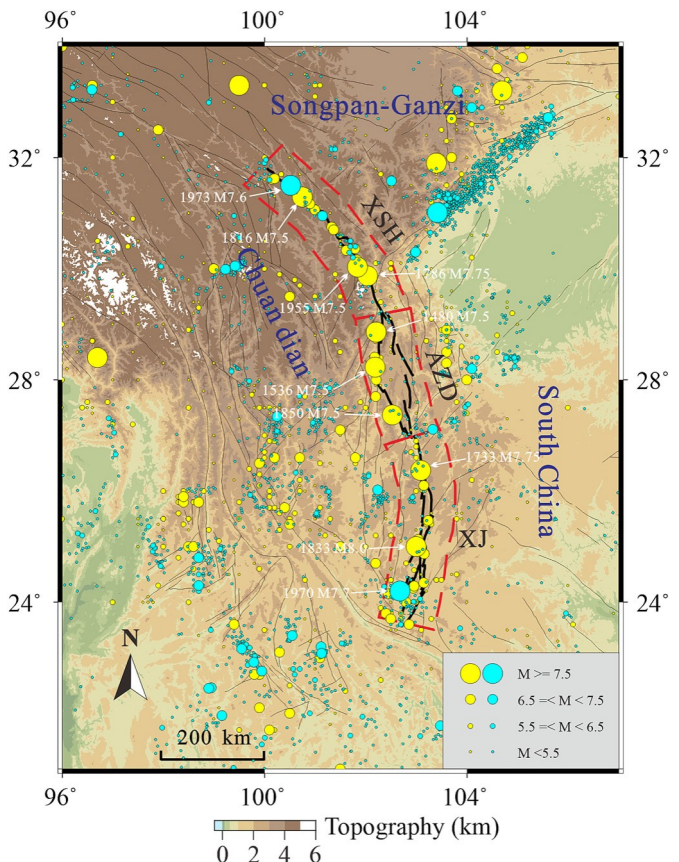


Fig. 3. GPS site velocities (blue arrows) with respect to the stable South China in the Chuandian region. Data are from Wang and Shen (2020). (For interpretation of the references to colour in this figure legend, the reader is referred to the web version of this article.)

Tibetan Plateau and an integrated earthquake catalog in the region. First, we calculated the moment rate from geodetic data for each seismic zone of the XXFS. Second, we compared the geodetic moment accumulation rate with the moment release rate, estimated by the Gutenberg-Richter (G-R) distribution method and the Kostrov moment summation method. Finally, we investigated the spatial distribution of moment deficits along the XXFS and identified six fault segments with moment deficit.

2. Tectonic setting

The arc-shaped XXFS is a major sinistral strike-slip fault system in the southeastern Tibetan Plateau, serving as the boundary among the Chuandian, Songpan-Ganzi, and South China blocks (Fig. 1a; Affen et al., 1984; Affen et al., 1991; Tappin et al., 2001; Xu et al., 2003; Zhang, 2013). It controls crustal extrusion and seismic activity in this region. The XXFS consists of three major fault zones: the Xiangshuihe (XSH) fault zone in the north, the Anninghe-Zemuhe-Dafliangshan (AZD) fault zone in the middle, and the Xiaojiaoliang (XJ) fault zone in the south (Fig. 1a).

From north to south, the XSH fault zone can be divided into five main segments by fault-trace discontinuities: the Luhuo (LH), Daofu (DF), Qianming (QN), Kangding (KD), and Moxi (MX) segments (Fig. 1b). The KD segment includes three right-stepping branches: the Yaflahe (YLH), Seflaha (SLH), and Zheduotang (ZDT) branches (Fig. 1b; Bafi et al., 2018; Qiao and Zhou, 2021). Geologic evidence indicates the strike-slip rate of the XSH fault in the range of 9–15 mm/yr since the late Quaternary (Affen et al., 1991; Xu et al., 2003; Zhang, 2013), consistent with the geodetic slip rate of 7–13 mm/yr (e.g., Shen et al., 2005; Wang et al.,

2017; Zheng et al., 2017; Wang and Shen, 2020). The high slip rate on the XSH fault zone has been associated with frequent big earthquakes (Fig. 2 and Table S1; Wen et al., 2008). Therefore, seismic hazard of the XSH fault has been a major concern.

The AZD fault zone includes the Annfinghe (ANH) and Zemuhe (ZMH) faults in the west and the Dafliangshan (DLS) fault in the east (Fig. 1c). The DLS fault is a young fault (< 4 Ma) with slow seismicity and no major earthquakes in the past several hundred years (Fig. 2; He et al., 2008; Wen et al., 2008). Both paleoseismic and geological studies found that seismicity on the DLS fault is significantly lower than that on the ANH and ZMH faults (Song et al., 2002; Zhou et al., 2003; Han and Jiang, 2005). Therefore, for the AZD seismic zone, our analysis includes only the ANH and ZMH faults. Geological investigations have shown that both the ANH and ZMH faults have left-lateral strike-slip rates of 4–8 mm/yr (Xu et al., 2003; He and Oguchi, 2008; Ran et al., 2008). The geodetic slip rates on the ANH and ZMH faults are within the range of 2–11 and 5–9 mm/yr, respectively (Shen et al., 2005; Wang et al., 2008; Wang et al., 2017).

The ANH fault has had two $M > 7.0$ events since 1480 CE: the 1480 M 7.5 earthquake in the northern part and the 1536 M 7.5 earthquake in the southern part (Fig. 2 and Table S1; Wen, 2000; Ran et al., 2008; Wen et al., 2008; Wang et al., 2014). The ZMH fault has had only one large earthquake ($M > 7.0$) since 1480 CE: the 1850 M 7.5 earthquake (Fig. 2 and Table S1; Wen, 2000; Wen et al., 2008).

The XJ fault zone in the southern part of the XXFS (Fig. 1a) has its northern segment connected to the ZMH and DLS faults. Its central and southern segments bifurcate into two subparallel branches separated by a distance of ~20 km (Fig. 1d). Geological and geodetic slip rates on the XJ fault are in the range of ~5–16 mm/yr (Honglin et al., 2002; Shen et al., 2005; He and Oguchi, 2008; Wang et al., 2017). Eight large earthquakes ($M > 7.0$) have occurred in the XJ fault zone since 1480 CE (Fig. 2; Table S1; Wen et al., 2008).

3. Data and methods

3.1. The integrated earthquake catalog and seismic moment release rate

3.1.1. The integrated earthquake catalog

China has nearly 3000-year-long earthquake records listed in various catalogs. The main catalogs include The Catalog of Chinese Historical Strong Earthquakes (Mfin et al., 1995), the Catalog of Chinese Recent Earthquakes (Wang et al., 1999), and the online catalog from the China Earthquake Networks Center (CENC; <https://www.cenc.ac.cn>). The Catalog of Chinese Historical Strong Earthquakes includes 1034 events of $M_s \geq 4.7$ in China from 2300 BCE to 1911 CE (Mfin et al., 1995). The earthquakes in this catalog were mainly based on historical documents of earthquake shaking and damage. The Catalog of Chinese Recent Earthquakes contains 4289 earthquakes of $M_s \geq 4.7$ from 1912 CE to 1990 CE (Wang et al., 1999). The online CENC catalog includes >10,000 $M \geq 4.0$ instrumentally recorded earthquakes that occurred in China and its surrounding areas since 1970 CE.

We combined the three catalogs to generate an integrated catalog. Because the Catalogs of the Chinese Recent Earthquakes and the Chinese Online Earthquakes have a time overlap, we used the events from 1912 CE to 1969 CE from the Chinese Recent Earthquakes and events from 1970 CE to the present from Chinese Online Earthquakes. From this integrated catalog we extracted the seismic events of $M \geq 4.0$ in the Chuanbian region (96–107° E, 21–34° N). The big earthquakes ($M \geq 6.5$) occurred mainly in the boundary fault zones, especially in the XXFS (Fig. 2). The magnitudes in these three catalogs were mainly expressed in M_s . We converted the M_s magnitude into moment magnitude (M_w) by using the regression relationships from Cheng et al. (2017) (Table S1).

The first recorded event within the XXFS region is dated to 1332 CE (Mfin et al., 1995). The historical seismic catalog generally lacks small events and may have missed some large events. The instrumentally recorded catalog is more complete but is short and may not have

recorded characteristic large earthquakes. We extracted events of $M > 6.0$ from a ~110-km swath along the XXFS (Fig. 2) for our analysis (Table S1). Wen et al. (2008) suggested that major earthquakes ($M > 6.0$) in the eastern boundary of the Chuanbian block are frequent and can be considered almost complete over the past centuries.

3.1.2. Seismic moment release rate

We used two methods to estimate the seismic moment rate from the integrated seismic catalog. The first method is the truncated cumulative G-R distribution (Hyndman and Wefchert, 1983):

$$\dot{M}_0 = \frac{1}{T} \varphi \frac{b}{c - b} 10^{(c - b) M_{\max} + a + d} \quad (1)$$

$$M_0 = 10^{(c \times M_w + d)} \quad (2)$$

where T is the time length, M_{\max} is the magnitude of the largest truncated earthquake within each seismic zone or maximum moment magnitude of each seismic zone, φ is a correction for the stochastic magnitude-moment relation, and a , b , c and d are input coefficients. φ is assumed to be 1.27 (Hyndman and Wefchert, 1983). The c and d are the coefficients of the magnitude (M_w) – scalar moment (M_0) relation (Eq. (2)), and we set $c = 1.5$ and $d = 9.05$ (Hanks and Kanamori, 1979). The a and b are the coefficients (intercept and slope, respectively) in the Gutenberg–Richter relation:

$$\log N = a - bM \quad (3)$$

where N is the cumulative number of earthquakes with magnitude $\geq M$. The values of a and b are calculated using the maximum likelihood method (Akaike, 1965; Wefchert, 1980; Shih and Boft, 1982) based on earthquakes from the integrated catalog (1480–2020 CE) in each seismic zone. The moment rate calculated by this method is referred to as the G-R moment rate.

The second method is the Kostrov moment summation (Kostrov, 1974). In this method, the seismic moment rate is obtained by the moment summation of the recorded earthquakes and averaged over the time length:

$$\dot{M}_0^s = \frac{1}{T} \sum_j M_0^j \quad (4)$$

where j is the j -th event in the earthquake catalog that occurred during a given time length T in each fault zone, and M_0^j is the scalar seismic moment of the j -th event. The moment rate calculated by this method is referred to as the KMS moment rate.

Theoretically, the truncated cumulative G-R distribution method (Eq. (1)) can estimate the moment release rate of seismic events for all magnitude ranges, assuming the Gutenberg–Richter relation of magnitude and number of earthquakes. It has the advantage of estimating the moment rate from events below the complete magnitude and is better suited to provide the long-term moment release rate (Sparacino et al., 2020; Ojo et al., 2021), but could be biased if the catalog does not allow accurate estimate of the M_{\max} and the parameters of the G-R relation. In contrast, the Kostrov moment summation makes no distribution assumption. It estimates moment release rate from the recorded earthquakes, thus may suffer from the incompleteness of the earthquake catalog.

3.2. GPS velocity data and geodetic moment accumulation rate

3.2.1. GPS velocity data and strain rate estimation

In this study, we used the latest GPS velocity results from Wang and Shen (2020). The GPS data sets are from multiple sources including the Crustal Movement Observation Network of China (CMONOC) project, the densified regional campaign GPS network, and regional continuous GPS sites (e.g., Shen et al., 2005; Wang et al., 2017; Zheng et al., 2017;

(Wang and Shen, 2020). Data time spans from 1991 CE to 2016 CE, and the longest time series data are >4 years. The GPS data comprise 543 horizontal velocity vectors throughout the Chuanbian region, with a high spatial density of $\sim 3.8 \times 10^{-4} \text{ km}^2$ on average (Fig. 3). The XXFS has the highest spatial density of $\sim 8-12 \times 10^{-4} \text{ km}^2$ (Fig. 3), indicating adequate solution of the strain rate field along the XXFS. The effects of co- and post-seismic deformation of large earthquakes were removed to derive a secular (interseismic) velocity solution (Wang and Shen, 2020).

Fig. 3 shows the GPS velocity field with respect to the stable South China block. The Chuanbian block moves faster than the neighboring Songpan-Ganzi and South China blocks. The velocity field is characterized by clockwise rotation of the Chuanbian block (Fig. 3), with a sharp drop in velocities across the XXFS. It indicates the importance of the XXFS in accommodating deformation and controlling the crustal extrusion of the Chuanbian block.

We estimated the horizontal strain rates on a regular $0.02^\circ \times 0.02^\circ$ grid over the investigated area by using the method of Shen et al. (2015). This method allows users to use different spatial weighting functions of the data. We calculated the horizontal strain rate fields by using a Gaussian function for distance weighting and Voronoi cell for area weighting. To balance the tradeoff between the resolution and robustness, we used a weighting threshold (Wt) of 18 with uncertainty of ± 6 . More discussion of selecting Wt is given below (Section 5.1).

3.2.2. Geodetic moment accumulation rate

The calculated strain rate field was used to estimate the geodetic moment accumulation rates. Following Ward (1998), we used the summation of the largest eigenvalue of the strain rate tensor:

$$\dot{M}^G = 2\mu AH \times \frac{1}{n} \sum_{i=1}^n \text{Max} \left(\frac{\varepsilon_1^2 + \varepsilon_2^2 + \varepsilon_3^2}{\varepsilon_1 \varepsilon_2 \varepsilon_3} \right) \quad (5)$$

where \dot{M}^G is the geodetic moment rate; μ and H are the shear modulus and depth of the seismogenic layer, respectively; A is the surface area of each fault zone; ε_1 and ε_2 are the absolute eigenvalues of the strain rate tensor (or two horizontal principal strain rates) within the grid inside the limits of each investigated zone.

4. Results

4.1. Strain and moment rates from GPS data

Fig. 4a shows the velocity field with respect to the stable South China, derived from a Gaussian fitting of the GPS site velocities. The velocity gradients were used to calculate strain rates (Fig. 4b). It shows that the shear strain rate is highly concentrated along the XXFS.

The maximum principal strain rates ($\text{Max} \frac{\varepsilon_1 + \varepsilon_2 + \varepsilon_3}{\varepsilon_1 \varepsilon_2 \varepsilon_3}$) on the grids

were averaged over each fault zones to calculate the average strain rate (Eq. (5)). The XSH seismic zone has the highest average strain rate ($42.3 \times 10^{-13} \text{ /yr}$), and the average strain rates gradually decrease southward to the AZD and XJ seismic zones (Table S2). The strain rate pattern is consistent with those derived from block or finite element models (Wang et al., 2011; Li et al., 2019; Wang and Shen, 2020; Yfin and Luo, 2021).

The geodetic moment rates (\dot{M}^G) for the three fault zones, calculated by Eq. (5), are shown in Tables 1 and S1. Because the focal depths of most (> 80%) earthquakes on the XXFS are above 20-km depth (Fig. S1),

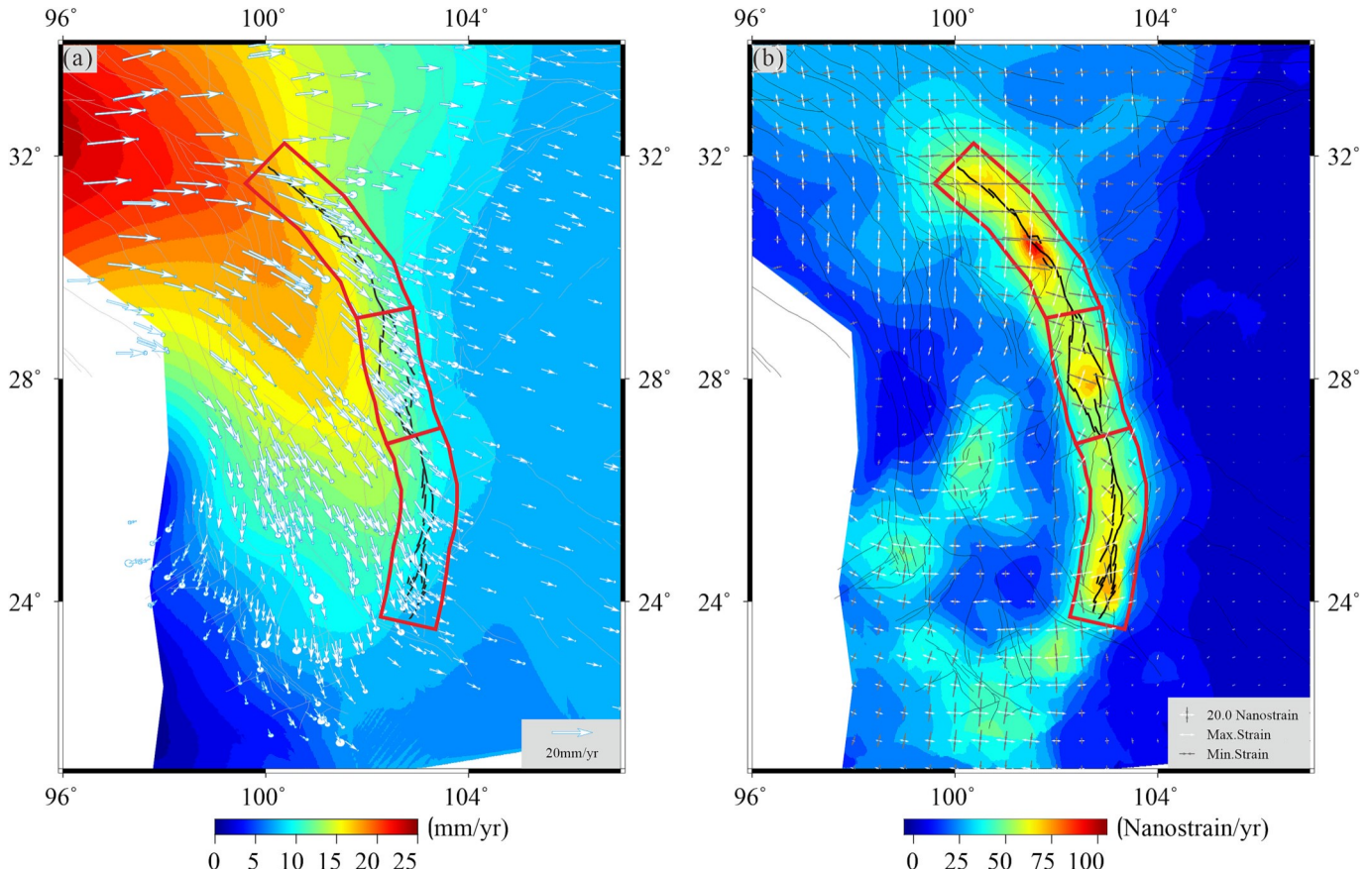


Fig. 4. GPS velocities and strain rates. (a) GPS site velocities (white arrows) with respect to the stable South China, and the continuous velocity field (color contours). (b) Strain rate (second invariant of the strain rate tensor) and principal strain rate (white and gray bars). The red polygonal regions are the seismic zones analyzed. (For interpretation of the references in this figure legend, the reader is referred to the web version of this article.)

Table 1

Geodetic moment rates (\dot{M}^G) and seismic moment rates estimated by the G-R method (G-R rate) and the KMS method (KMS rate).

Zone	\dot{M}^G ID	G-R rate 10^{17} (Nm/ yr)	KMS rate 10^{17} (Nm/ yr)	Rafito G-R rate/ \dot{M}^G	Rafito KMS rate/ \dot{M}^G
XSH	21.3 ^{+10.2} 7.2	16.4 ^{+38.3} 11.5	14.9	0.77 ^{+3.11} 0.61	0.7 ^{+0.36} 0.23
AZD	10 ⁺⁴ 3.1	2.6 ^{+5.4} 1.8	7.6	0.26 ^{+0.9} 0.2	0.76 ^{+0.34} 0.22
XJ	12.9 ^{+5.3} 4.4	24.8 ^{+49.7} 16.6	24.8	1.92 ^{+6.84} 1.47	1.92 ^{+1.0} 0.56

we took H to be 20 km with an uncertainty of ± 5 km. The XSH seismic zone has the highest geodetic moment accumulation rate of the three seismic zones, roughly twice that of the AZD and XJ seismic zones (Tables 1 and S2).

4.2. Rates of seismic moment release

As mentioned above, we calculated the rates of seismic moment release using two methods. The G-R moment rates, calculated using the truncated cumulative G-R distribution (Eq. (1)), are shown in Tables 1 and S3. The input parameter M_{\max} , taken to be the maximum magnitude observed in each fault zone, is $M_w \sim 7.7$, $M_w 7.5$, and $M_w 8.0$ in the XSH, the AZD, and the XJ seismic zone, respectively (Table S3). The a and b values were calculated from the integrated seismic catalog that dates from 1480 CE to 2020 CE, using the ZMAP code with maximum likelihood method (Fig. S2; Wiemer, 2001).

We also used the Koström moment summation method (Eq. (4)) to calculate the moment release rate (KMS moment rate) for seismic events of $M_w > 6.0$. The moment release is summed over each fault zone and averaged over 540 years (1480–2020 CE) for the moment release rate (Table S3). Events below $M_w 6.0$ are incomplete in the integrated seismic catalog, and the moment rate derived from small earthquakes ($M \leq 6.0$) accounts for <10% of that from major earthquakes. Therefore, we have ignored the contributions of small earthquakes in calculating the KMS moment rate. Table S1 lists the magnitude and moment release of each major earthquake ($M_w > 6.0$) since 1480 CE.

The KMS moment rates are close to the G-R moment rates for the XSH and XJ seismic zones (Table 1); however, the KMS moment rate for the AZD seismic zone (7.6×10^{17} Nm/year) is more than three times higher than the G-R moment rate (2.6×10^{17} Nm/year). The lower G-R moment rate may be caused by underestimating the M_{\max} ($M_w 7.5$) of the AZD seismic zone. A higher M_{\max} would raise the estimated G-R rate. Another reason may be the inadequate number of major earthquakes ($M > 6.0$), which could lead to underestimate values of a and b , hence a lower G-R moment rate.

4.3. Moment balance

The geodetic moment rate includes both elastic and inelastic components of the loading, while the seismic moment rate reflects the elastic unloading by earthquakes. The first comparison thus could provide valuable information of energy balance and earthquake potential on seismic fault zones (e.g., Hanks and Kanamori, 1979; Sparacino et al., 2020). Theoretically, the ratio between long-term averaged seismic moment rate and geodetic moment rate ranges from zero to one. A ratio close to one indicates that most of the accumulated strain has been released by earthquakes (D'Agostino, 2014), thus the energy budget of accumulation and release is nearly balanced. In contrast, a low ratio indicates an apparent seismic moment deficit, which may be attributed to some aseismic deformation or strain energy to be released by future earthquakes (Meade and Hager, 2005; Sparacino et al., 2020). The ratio could exceed one (seismic moment rate is larger than geodetic moment rate) if the seismic catalogs are too short and contain one or more large earthquakes (Paolano et al., 2018; Sparacino et al., 2020). A seismic

catalog has to cover one or more seismic cycles to provide a reliable estimate of the long-term seismic moment release rate.

The ratios of seismic moment release rate (G-R moment rates in Table 1) to the geodetic moment accumulation rate (\dot{M}^G in Table 1) are 0.77 (0.16–3.88) and 1.92 (0.45–8.76) for the XSH and XJ seismic zones, respectively. The results are similar when using the KMS moment rate (Table 1). For the AZD seismic zone, the KMS moment rate is preferred to the G-R moment rate, which may be an underestimate due to the inadequate large earthquakes in the catalog. The ratio is 0.76 (0.54–1.1) for the AZD seismic zone. Thus, strain energy is mostly released by earthquakes within the XSH and AZD seismic zones. The larger-than-one ratio for the XJ fault zone indicates that the time length (540 years) cannot fully capture one complete seismic cycle there.

More detailed comparison of seismic and geodetic moment rates is presented in Fig. 5 for the three seismic zones. Fig. 5a shows that, since 1480 CE, the accumulated geodetic moment in the XSH seismic zone has been largely released by several $M > 7.0$ earthquakes. No large earthquakes were recorded before 1700 CE. If this is not due to missing events but reflects temporally clustered seismicity (Chen et al., 2020), then the comparison indicates a seismic moment deficit up to $\sim 2.49 \times 10^{20}$ Nm ($1.396 \sim 8 \times 10^{20}$ Nm), equal to an earthquake of $M_w \sim 7.5$.

The AZD seismic zone has had relatively slow seismic activity, including only six $M > 6.0$ earthquakes since 1480 CE (Fig. 5b). Seismic moment since 1480 CE was mostly released by three $M_w 7.5$ earthquakes. Comparison with geodetic moment accumulation over the same period shows a moment deficit of $\sim 1.28 \times 10^{20}$ Nm ($0.9 \sim 2.93 \times 10^{20}$ Nm), which equals an $M_w \sim 7.4$ earthquake.

The XJ seismic zone shows a moment surplus (Fig. 5c). Most seismic moment release since 1480 CE was by the few $M > 7.5$ earthquakes, and the 1833 $M_w 8.0$ event accounted for $\sim 60\%$ of the total moment release during this period. These results suggest a relatively slow hazard in the near future.

4.4. Spatial distribution of moment budget

Our results suggest overall moment deficits in the XSH and AZD but a moment surplus in the XJ seismic zones. Here, we compare the spatial distribution of moment accumulation and release along the XXFS (Fig. 6). The rupture zone of each event is from previous field studies (e.g., Wen et al., 2008; Yfi et al., 2015) or calculated from an empirical magnitude-fault length scaling relationship for strike-slip faults (Wells and Coppersmith, 1994). The centers of the rupture zones are assumed to be the epicenters of earthquakes (Fig. 6b).

To obtain the spatial distribution of seismic moment release, the moment of each event is smoothed using a Gaussian function, whose center is located at the macroseismicity determined epicenter and whose 4σ width equals the estimated fault length (D'Agostino, 2014). The contributions of the macroseismic events are numerically integrated to estimate the seismic moment release in various time frames (Fig. 6c).

The geodetic moment within each seismic zone is obtained by the total geodetic moment accumulated since 1480 CE (Table 1) divided by the fault length. Fig. 6c shows that some regions have released the accumulated moment, such as the northern part of the DF and the southern parts of the KD segments, the ANH fault segment, and the central ZMH fault segment. The XJ fault has a moment surplus mainly due to the 1833 $M_w 8.0$ and 1733 $M_w 7.75$ events, causing seismic moment release on most of this fault to exceed the accumulated moment since 1480 CE.

Fig. 6 also indicates six seismic gaps marked by notable moment deficits. The northernmost one is located at the LH segment of the XSH fault. Although three major earthquakes (the 1811 $M_w 6.75$, 1967 $M_w 6.8$, and 1973 $M_w 7.6$ events) occurred here, it still has a significant seismic moment deficit (Fig. 6c). The next gap to the south is located at the QN and northern KD segments, where only one $M_w 7.0$ event occurred in 1893. Other gaps are found in the southern part of the MX segment on

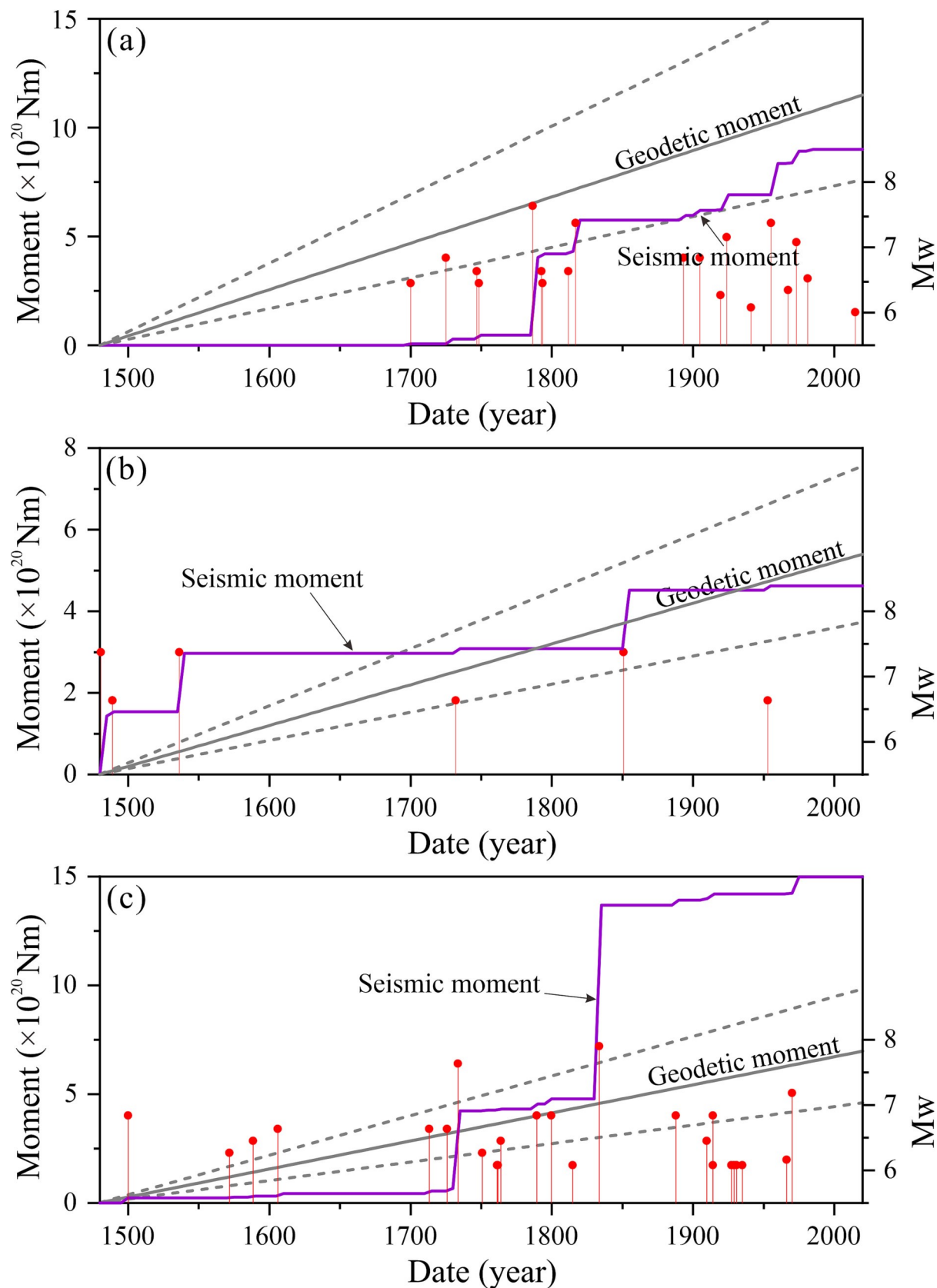


Fig. 5. Cumulative seismic moment (purple line) calculated by Kostrv moment summation of major earthquakes ($M > 6.0$; red dots). (a) the XSH seismic zone. (b) the AZD seismic zone. (c) the XJ seismic zone. The geodetic moment budget is shown by the gray line with uncertainty (gray dashed lines). (For interpretation of the references to colour in this figure legend, the reader is referred to the web version of this article.)

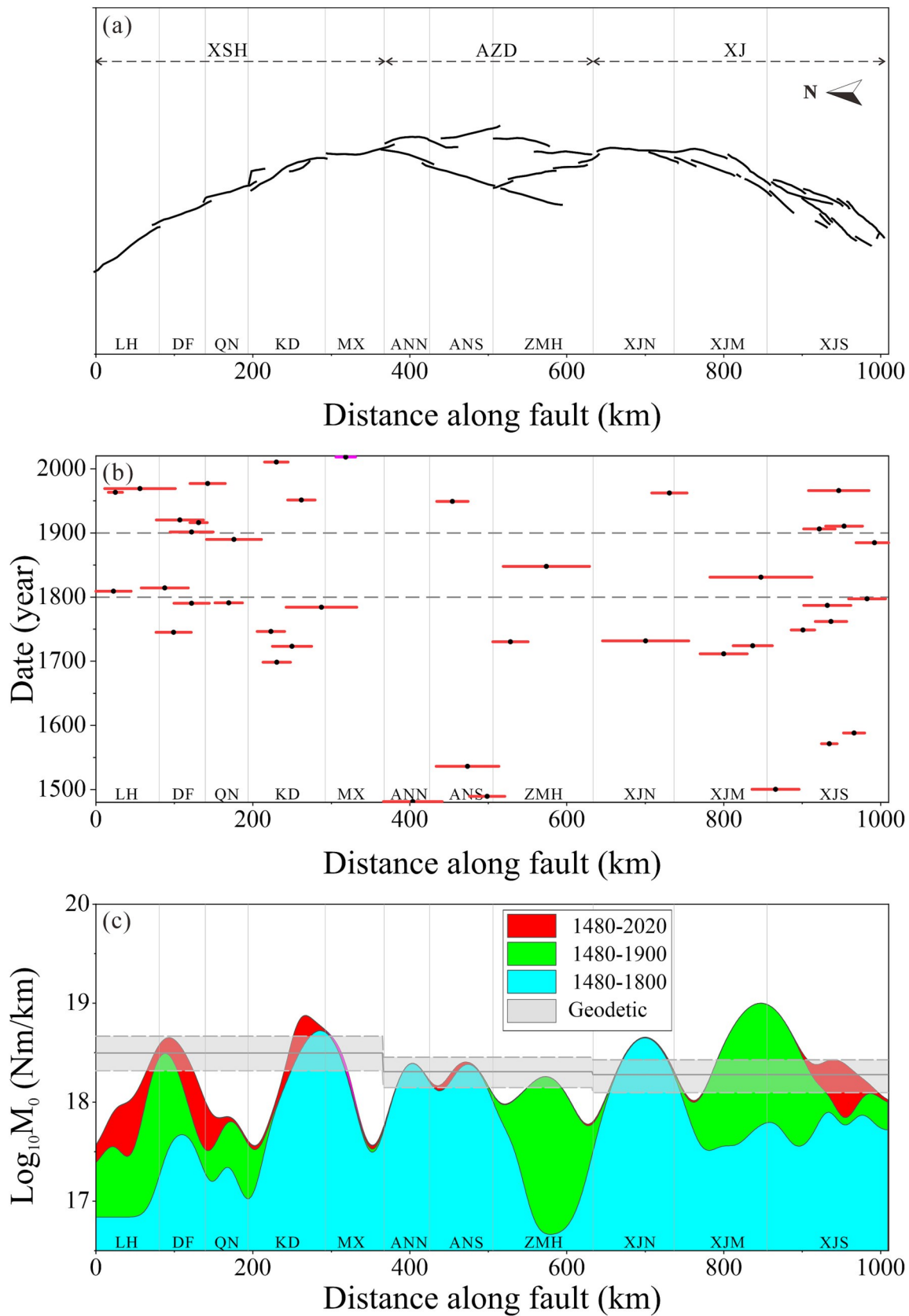


Fig. 6. (a) Fault traces of the XXFS. (b) Major events ($M_W > 6.0$) ordered in temporal sequence from bottom to top, shown as horizontal red bars scaled to the length of fault rupture. (c) Distribution of the smoothed seismic moment release in various time frames (colored areas) compared with the geodetic moment build-up from 1480 CE to 2020 CE (gray dashed and solid lines). Uncolored areas below the geodetic moment lines indicate moment deficits. Abbreviations are explained in Fig. 1. (For interpretation of the references to color in this figure legend, the reader is referred to the web version of this article.)

the XSH fault and the northern part of the ANH fault, northern part of the ZMH fault, the segment between the ZMH segment and the northern part of the XJ segment, and the northern end of the central XJ fault (Fig. 6c). It is also clear from Fig. 6c that large earthquakes since 1800 CE generally occurred in segments of moment deficit, gradually filling up the moment deficits. This pattern indicates that moment deficits may be a good indicator for future large earthquakes in the XXFS.

4.5. Seismic potential along the XXFS

To assess the potential seismic hazard along the fault system, we set a spatial window and move it along each fault zone to calculate the accumulated moment deficit within the window between 1480 CE and 2020 CE (Figs. 7–9). The length of the spatial window depends on the investigated moment magnitude, which is according to the relationship between the rupture length and magnitude (Wells and Coppersmith, 1994). For example, to see which parts of the XXFS may generate earthquakes of M_w 6.5, we set a spatial window of 24 km and calculate the accumulated moment deficit within the window. The calculated total moment deficit is assigned to the center of the window. If the accumulated moment deficit within the window exceeds the moment of an earthquake of M_w 6.5, the fault within the window is considered capable of producing an earthquake of M_w 6.5. We move the window from north to south along the fault zones with a moving step of 1 km to obtain a one-dimensional curve of accumulated moment deficit along each seismic zone. Similarly, we used two larger windows for potential larger earthquakes (50 km for M_w 7.0 and 94 km for M_w 7.4 events) (Figs. 7c, 8c and 9c).

Fig. 7c compares the accumulated moment deficits within the moving windows along the XSH seismic zone. The spatial windows of 24, 50 and 94 km correspond to M_w 6.5, 7.0 and 7.4 earthquakes, respectively. Along-strike length, ~69% of the fault there has enough accumulated strain (blue regions in Fig. 7c) to release an earthquake of M_w 6.5, and these fault sections are all within the three seismic gaps. About ~58% and ~27% of the fault zone are capable of producing an event of M_w 7.0 (green regions) or 7.4 (red regions), respectively. The potential of an event of M_w ~7.4 is concentrated in a wide region along the QN and KD segments of the XSH fault. This is consistent with the previous result of elastic block modeling that suggested fault slip deficits along this segment for an earthquake of M_w 7.1 (Wang et al., 2010).

The AZD seismic zone has three sections with remarkable moment deficits: one at the northern end of the ANH fault and two at the ends of the ZMH fault (Fig. 8a and b), and all have the potential to produce an earthquake of M_w 6.5 (blue region in Fig. 8c). At both ends of the ZMH fault, the deficits could also produce an earthquake of M_w 7.0 (Fig. 8c). Fig. 8c shows that the AZD seismic zone does not have enough deficits for an earthquake of M_w 7.4. However, this should be treated with caution, because no large earthquake ($M > 7.0$) has occurred at the ANH fault since the 1536 M7.5 event (Fig. 6b and Table S1). Within ~500 years of elapsed time, the ANH fault could have a high risk of large earthquakes.

The XJ fault has the most complex fault structure along the XXFS (Fig. 9a). Because much of the accumulated moment has been released by the 1733 M 7.75, 1833 M 8 and the 1970 M 7.7 earthquakes, most parts of the XJ fault have moment surplus (Fig. 9b). Some sections of the XJ show moderate moment deficits that may produce M_w 6.5 earthquakes (Fig. 9c). However, the middle segment of the XJ fault has not experienced any major earthquake since the 1833 M 8.0 event (Fig. 6b and Table S1). Similarly, the last major event in the northern XJ fault was the 1733 M 7.75 earthquake (Fig. 6b and Table S1). These places deserve further study.

5. Discussion

5.1. Uncertainties in estimation of the moment and rate

We have provided a detailed analysis of moment budget along the XXFS using an integrated catalog and the latest GPS measurements. The estimate of geodetic moment rate can be affected by factors such as the selected width of the seismic zone, the thickness of the seismogenic layer (H), and the smooth method in computing the strain rates from the GPS velocity field. We set H to 20 ± 5 km based on the observed regional seismic focal depth along the XXFS (Table 1). This value is close to the fault locking depth (17 km) of the XSH obtained from elastic block model by Wang et al. (2010) and fault locking depth (21 km) in the Tibetan Plateau (Wang et al., 2011). Additional constraints of fault locking depth are provided by earthquake focal depths. Relocation of major earthquakes in the Tibetan Plateau indicates the focal depths of most events to be shallower than 25 km (Yang et al., 2005). In addition, we found the focal depths from the seismic catalog in our study are mostly (>80%) located shallower than 20 km (Fig. S1).

The width of the seismic zone is selected to be 110 km, because the high strain rates (~25–100 nanostrain/yr) are mainly distributed within 110 km across these fault zones (Fig. 2b). Previous studies have shown that high strain rates are concentrated within tens of kilometers on both sides of large strike-slip faults (e.g., Tape et al., 2009; Shen et al., 2015; Ili et al., 2018; Wang and Shen, 2020; Ili et al., 2021). Zhao et al. (2021) assumed wider seismic zones along the XSH, AZD and XJ faults than those in our study. We also test wider seismic zones with 150-km width. The geodetic moment rate increases of ~26%, 23% and 20% are obtained in the XSH, AZD and XJ seismic zone, respectively. They remain within the uncertainty range of the geodetic moment rate (Table S2). Increasing the width of the seismic zones would increase the moment rate but does not change our main results.

The smooth strategies can affect the strain rates computed from the GPS velocity field (e.g., Tape et al., 2009; Shen et al., 2015). We used the Gaussian function for distance-dependent weighting and the Voronoi cell area weighting function for spatially dependent weighting for flow (Shen et al., 2015). We tested the weighting threshold (W_t) from 12 to 30 (Fig. S3). Increasing W_t would smooth the strain rate field at the expense of spatial resolution, or the robustness, of the resolved strain rates (Shen et al., 2015). To balance the tradeoff between the resolution and robustness, we selected the model with $W_t = 18$ as the optimal model for characterization of the strain-rate field in the Chuanjian region (Figs. 4 and S3). The selection of W_t is consistent with the optimal value range in previous studies (Shen et al., 2015; Zhao et al., 2021).

The estimation of seismic moment release rate is also affected by several factors. A complete seismic catalog is most important for moment budget analysis. For the XXFS, the catalog is incomplete for events of $M < 6.0$. To investigate the influence of the incompleteness of the seismic catalog, we used both the methods of G-R distribution and Kostrov moment summation. A comparison of results from these two methods suggests that the $M < 6.0$ events potentially missing in the catalog contribute <10% of the total moment release.

The results can also vary with time span chosen for moment analysis because of the potential influence of incompleteness of the catalog. Wen et al. (2008) have found that, since 1327 CE, major earthquakes ($M > 6.0$) on the eastern boundary of the Chuanjian block have been frequent and can be considered almost complete for events above $M 6.0$. We estimated the complete magnitude (M_c) based on the integrated seismic catalog within each seismic zone (Fig. S2). The results show that earthquakes with magnitude above $M 6.0$ are complete since 1480 CE. Therefore, we choose to analyze the moment balance between 1480 CE and 2020 CE.

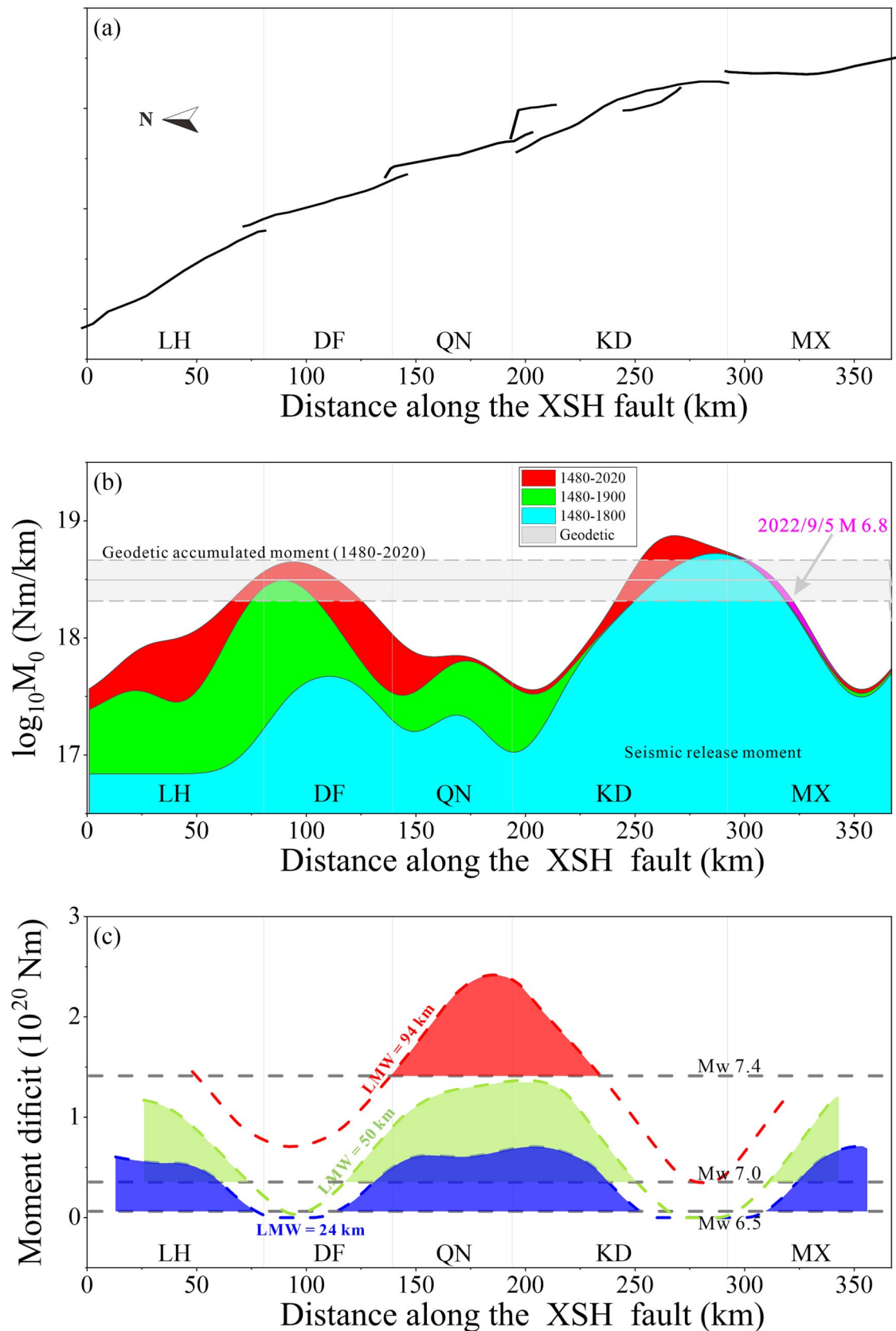


Fig. 7. Fault trace and moment deficits along the XSH fault. (a) Fault trace of the XSH fault. (b) Moment deficits indicated by comparison of the seismic and geodetic moment along the XSH fault (uncolored areas under the geodetic moment lines). (c) The accumulated moment deficits within a moving spatial window of 24 km (M_w 6.5), 50 km (M_w 7.0), and 94 km (M_w 7.4) along the XSH fault, assuming a zero-strain level at 1480 CE. Gray dashed lines are the corresponding earthquake moments. LMW: Length of moving windows.

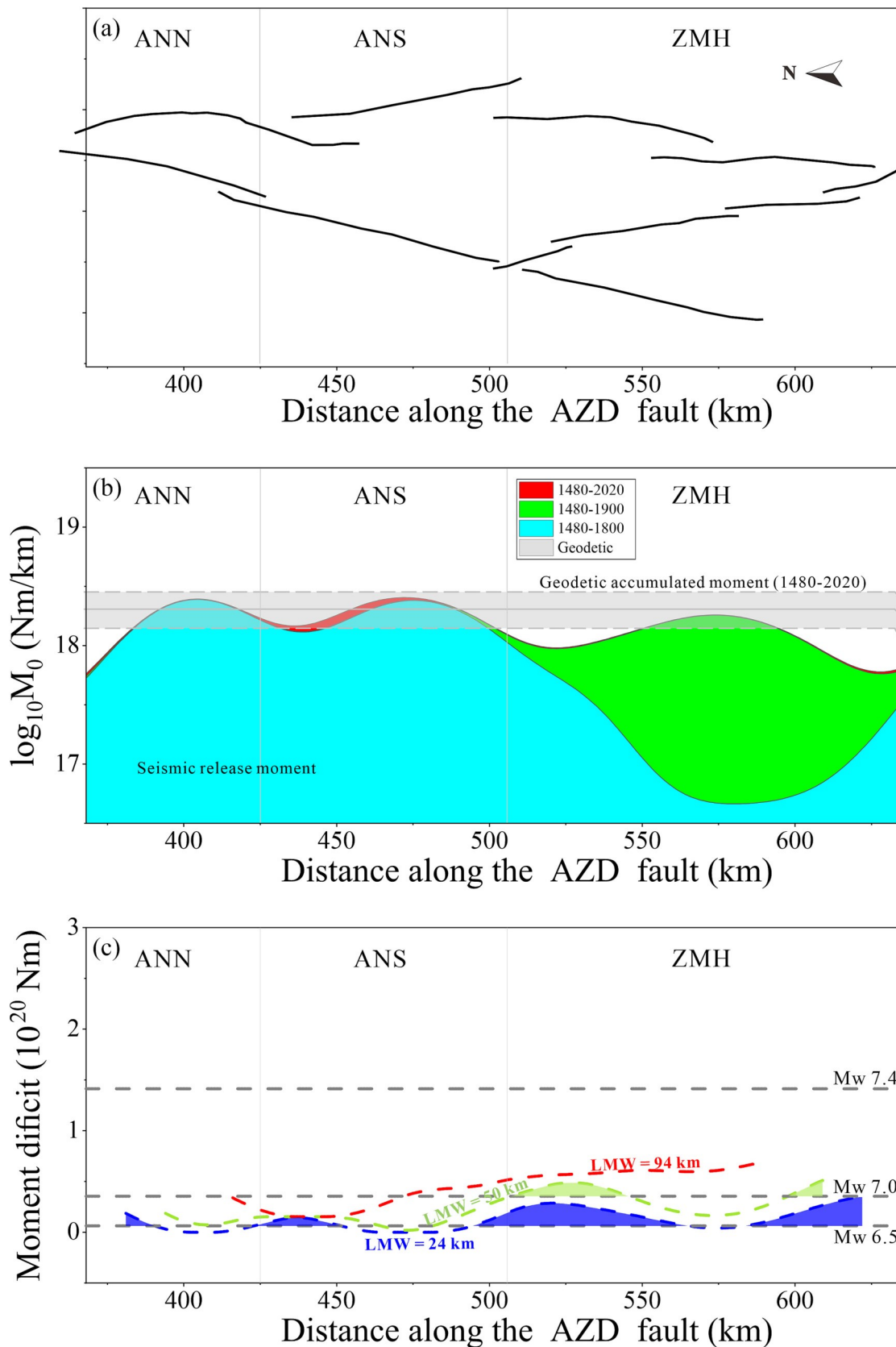


Fig. 8. Fault trace and moment deficit along the AZD fault. (a) Fault trace of the AZD fault. (b) Moment deficit fits indicated by comparison of the seismic and geodetic moment along the AZD fault (uncolored areas under the geodetic moment lines). (c) The accumulated moment deficit fits in a moving spatial window of 24 km (M_w 6.5), 50 km (M_w 7.0), and 94 km (M_w 7.4) along the AZD fault, assuming a zero-strain level at 1480 CE. Gray dashed lines are the corresponding earthquake moments. LMW: Length of moving windows.

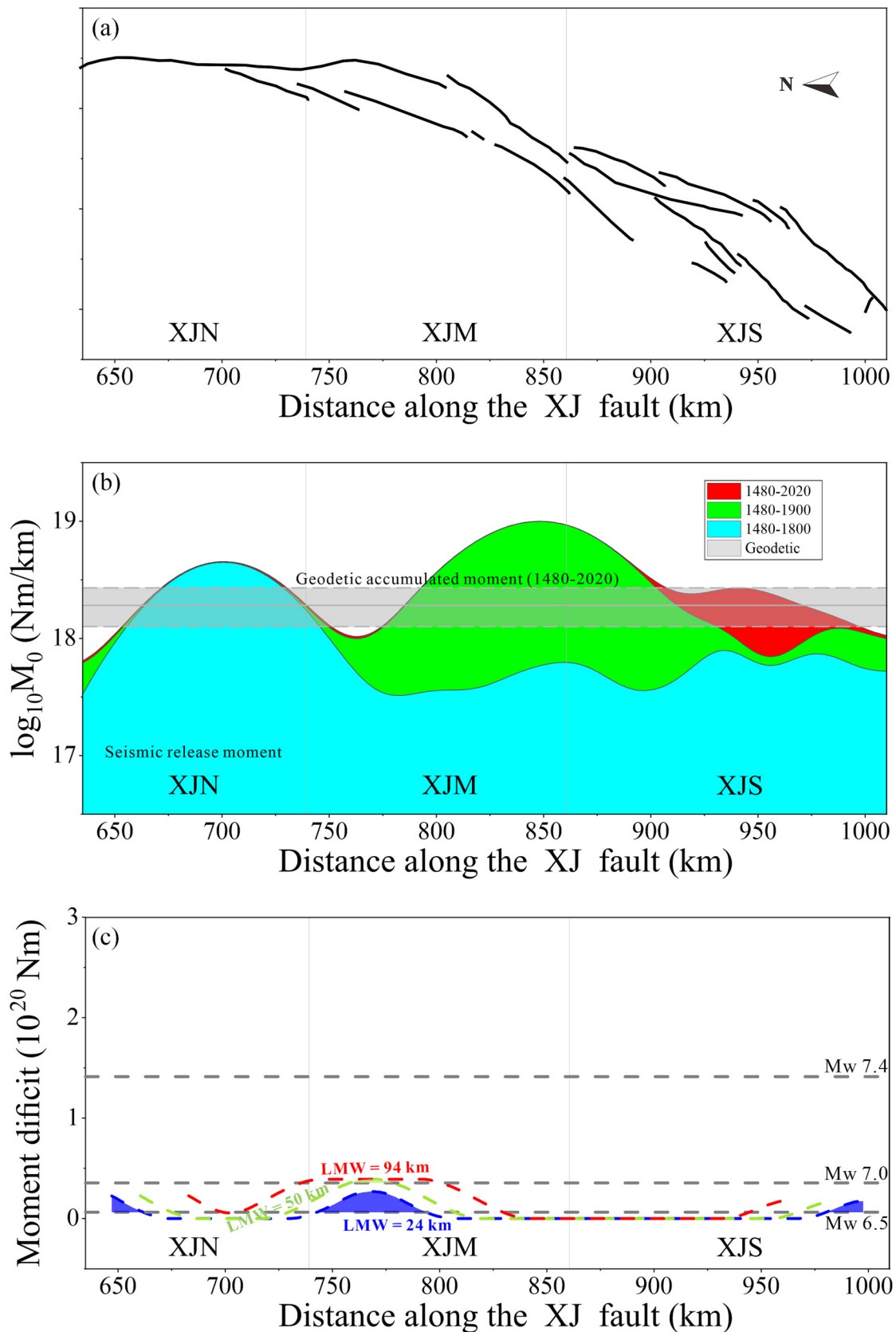


Fig. 9. Fault trace and moment deficit along the XJ fault. (a) Fault trace of the XJ fault. (b) Moment deficit indicated by comparison of the seismic and geodetic moment along the XJ fault (uncolored areas below the geodetic moment lines). (c) The accumulated moment deficit with a moving spatial window of 24 km (M_w 6.5), 50 km (M_w 7.0), and 94 km (M_w 7.4) along the XJ fault, assuming a zero-strain level at 1480 CE. Gray dashed lines are the corresponding earthquake moments. LMW: Length of moving windows.

5.2. Moment deficits and seismic hazard

Moment deficits may indicate energy available for future earthquakes if all strain energy is released seismically. However, aseismic deformation, such as fault creeping and afterslip, may also explain some of seismic moment deficits (Wesson, 1988; Maclerf et al., 2003; Hong and Liu, 2021). Previous studies have shown several shearflow (≤ 5 km) creeping sections along the XSH fault. For example, Ili and Bürgmann (2021) have found that the shearflow creep rate is up to 5 mm/yr around the 2014 Kangding event, and Qiao and Zhou (2021) found 16.3–19.8 mm/yr shearflow creeping on the KD segment. Because the high creep rate on the KD segment is postseismic and decreases rapidly, it contributes only a small portion to the total accumulated moment deficits along the KD segment. Other fault segments also show small values in postseismic fault creep rates and rapidly decrease after earthquakes (Zhang et al., 2018). The same can be said for the observed creeping on the QN and MX segments (Ili and Bürgmann, 2021; Qiao and Zhou, 2021). Because of the shearflow creep depth (~ 2 km) (Qiao and Zhou, 2021), even assuming a constant creep rate from 1480 CE to 2020 CE, the moment released by fault creep is $\sim 4.0 \times 10^{17}$ Nm/km and $\sim 2.3 \times 10^{17}$ Nm/km on the QN and MX segments, respectively, <10% of the accumulated moment deficits on the QN ($\sim 43 \times 10^{17}$ Nm/km) and MX ($\sim 45 \times 10^{17}$ Nm/km) segments (Fig. 7b). Therefore, we conclude that aseismic deformation has significant influence on our moment balance analysis. Note that most large earthquakes since 1800 CE occurred within the fault sections of moment deficit (Fig. 6c), gradually filling up the deficit gaps. This spatiotemporal pattern suggests that moment deficits can be a useful indicator of the locations of future earthquakes along the XXFS.

We note that, while this paper was under review, an M 6.8 earthquake (the Luding earthquake) occurred along the northern segment of the Moxi (MX) fault, a section of moment deficit identified in the XSH fault zone (Fig. 6b-c). Taking this event into consideration, the southern part of the MX fault still has moment deficits capable of generating an M > 7.0 earthquake (Fig. 7b).

The moment deficits are mostly found in the connection parts of fault segments (Fig. 6c). It may be attributed to incomplete moment release near the fault discontinuities. Previous numerical models suggest that significant fault slip deficits can occur in fault discontinuities after multiple earthquake cycles (Sun et al., 2019). These fault discontinuities or irregularities could hamper cascade fault rupture (Wang et al., 2020), leading to the moment and slip deficits. On the other hand, ruptures of the earthquake sequence along the XXFS, indicated by previous studies (e.g., Shan et al., 2013; Luo and Liu, 2018; Yan et al., 2018; Ili et al., 2020), show that the Coulomb stress generally increases in the LH, QN-KD, MX segments where moment deficits have accumulated. While moment deficits may give an estimate of the maximum magnitude of future earthquakes, the Coulomb stress change can tell which fault segment has moved toward failure. Combining both pieces of information can provide a better hazard assessment than using either of them alone (Liu et al., 2014).

6. Conclusions

In this study, we presented a detailed comparison between seismic moment release calculated from an integrated seismic catalog and moment accumulation derived from the GPS velocity field along the Xianshuihe-Xiaojiang fault system in the southeastern Tibetan Plateau. Major conclusions we draw from this study include the following.

- 1) The Xianshuihe and Annninghe-Zemuhe seismic zones have apparent moment deficits of $\sim 2.49 \times 10^{20}$ (Nm) and $\sim 1.28 \times 10^{20}$ (Nm), respectively, since 1480 CE. They potentially could produce an $M_w \sim 7.5$ and $M_w \sim 7.4$ earthquake, respectively. In contrast, the Xiaojiang seismic zone has a significant moment surplus, therefore a relatively low hazard.

- 2) Six sections of moment deficits (or seismic gaps) have been found along the XXFS, including the northern Luhuo segment, the Qianfeng-Kangding segment, the Moxi segment, the southern segment of the Annninghe fault, the northern Zemuhe fault, and the connecting section between Zemuhe and Xiaojiang faults, and all can produce an M_w 6.5 event. Within the Qianfeng-Kangding segment, sufficient moment deficit has accumulated to produce an event as large as M_w 7.4. The Annninghe fault, where no major earthquakes have occurred since 1536 CE, deserves particular attention.
- 3) The fault sections of moment deficits along the Xianshuihe-Xiaojiang fault system are closely related to fault stepovers or geometric changes. However, the rupture histories indicate that earthquakes can rupture through these fault segments. Given that big earthquakes since 1480 CE mostly occurred in these sections in a trend to fill up the moment deficits, it is reasonable to expect future earthquakes to occur in these sections.

CRedit authorship contribution statement

Li Yin: Conceptualization, Methodology, Data curation, Visualization, Investigation, Writing – original draft. **Gang Luo:** Supervision, Writing – review & editing. **Mian Liu:** Supervision, Writing – review & editing.

Declaration of Competing Interest

The authors declare that they have no known competing financial interests or personal relationships that could be perceived as influencing the work reported in this paper.

Data availability

Data will be made available on request.

Acknowledgments

This research is supported by the National Key Research and Development Project of China (2022YFC3003501, 2021YFC3000605), the National Natural Science Foundation of China (41904089, 41974107, 41574085), Liu acknowledges support from NSF grant (2013656). We used GMT software (Wessel et al., 2019) to generate some figures in this paper and this software can be downloaded at <https://www.generic-mapping-tools.org/>.

Appendix A. Supplementary data

Supplementary data to this article can be found online at <https://doi.org/10.1016/j.tecto.2023.229935>.

References

Aki, K., 1965. Maximum likelihood estimate of b in the formula $N = a - bM$ and its confidence limits. *Bull. Earthq. Res. Inst. Tokyo Univ.* 43, 237–239.

Affen, C.R., Griffiths, A.R., Han, Y.A., Sieh, K.E., Zhang, B.C., Zhu, C.N., 1984. Red river and associated faults, Yunnan Province, China - Quaternary geology, slip rates and seismic hazard. *Geol. Soc. Am. Bull.* 95 (6), 686–700. [https://doi.org/10.1130/0016-7606\(1984\)95<686:Rraaf>2.0.co;2](https://doi.org/10.1130/0016-7606(1984)95<686:Rraaf>2.0.co;2).

Affen, C.R., Luo, Z.L., Qian, H., Wen, X.Z., Zhou, H.W., Huang, W.S., 1991. Field study of a highly active fault zone: the Xianshuihe fault of southwestern China. *Geol. Soc. Am. Bull.* 103 (9), 1178–1199. [https://doi.org/10.1130/0016-7606\(1991\)103<1178:Fsoaha>2.3.co;2](https://doi.org/10.1130/0016-7606(1991)103<1178:Fsoaha>2.3.co;2).

Bafi, M.K., Chevallier, M.L., Pan, J.W., Replumaz, A., Lefloup, P.H., Metofis, M., Ili, H.B., 2018. Southeastward increase of the late Quaternary slip-rate of the Xianshuihe fault, Eastern Tibet. Geodynamic and seismic hazard implications. *Earth Planet. Sci. Lett.* 485, 19–31. <https://doi.org/10.1016/j.epsl.2017.12.045>.

Chen, Y., Liu, M., Luo, G., 2020. Complex temporal patterns of large earthquakes: Devil's staircase. *Bull. Seismol. Soc. Am.* 110 (3), 1064–1076.

Cheng, J., Rong, Y., Magistrale, H., Chen, G., Xu, X., 2017. An Mw-based historical earthquake catalog for mainland China. *Bull. Seismol. Soc. Am.* 107 (5), 2490–2500. <https://doi.org/10.1785/0120170102>.

Chousianitis, K., Ganas, A., Evangelidis, C.P., 2015. Stratification and rotation rate patterns of mainland Greece from continuous GPS data and comparison between seismic and geodetic moment release. *J. Geophys. Res. Solid Earth* 120 (5), 3909–3931. <https://doi.org/10.1002/2014jb011762>.

D'Agostino, N., 2014. Complete seismic release of tectonic strain and earthquake recurrence in the Apennines (Italy). *Geophys. Res. Lett.* 41 (4), 1155–1162. <https://doi.org/10.1002/2014gl059230>.

Han, W., Jifang, G., 2005. Study on seismicity of Dafliangshan and Annfinghe-Zemuhe fault zones. *J. Seismol. Res.* 28 (3), 207–212.

Hanks, T.C., Kanamori, H., 1979. A moment magnitude scale. *J. Geophys. Res.* 84 (NB5), 2348–2350. <https://doi.org/10.1029/JB084fiB05p02348>.

He, H., Oguchi, T., 2008. Late Quaternary activity of the Zemuhe and Xiaojiaogang faults in Southwest China from geomorphological mapping. *Geomorphology* 96 (1–2), 62–85. <https://doi.org/10.1016/j.geomorph.2007.07.009>.

He, H.L., Ikeda, Y., He, Y.L., Togo, M., Chen, J., Chen, C.Y., Tajikara, M., Echigo, T., Okada, S., 2008. Newly-generated Dafliangshan fault zone - shortcircuiting on the central section of Xianshuihe-Xiaojiaogang fault system. *Sci. China Ser. D Earth Sci.* 51 (9), 1248–1258. <https://doi.org/10.1007/s11430-008-0094-4>.

Hong, S., Lifu, M., 2021. Postseismic deformation and afterslip evolution of the 2015 Gorkha earthquake constrained by InSAR and GPS observations. *J. Geophys. Res. Solid Earth* 126 (7) e2020JB020230.

Honglun, H., Ikeda, Y., Fangmin, S., Xingquan, D., 2002. Late quaternary slip rate of the Xiaojiaogang fault and its simplification. *Seismol. Geol.* 24 (1), 14–26.

Hyndman, R.D., Wefichert, D.H., 1983. Seismicity and rates of relative motion on the plate boundaries of Western North America. *Geophys. J. R. Astron. Soc.* 72 (1), 59–82. <https://doi.org/10.1111/j.1365-246X.1983.tb02804.x>.

Kostrov, B.V., 1974. Seismic moment and energy of earthquakes, and seismic flow of rock. *Izv. Acad. SSSR Phys. Solid Earth* 1, 23–44.

Ifi, Y., Bürgmann, R., 2021. Parafault coupling and earthquake potential along the Xianshuihe Fault, China. *J. Geophys. Res. Solid Earth* 126 (7). <https://doi.org/10.1029/2020jb021406>.

Ifi, Y., Lifu, M., Wang, Q., Cui, D., 2018. Present-day crustal deformation and strain in northeastern Tibetan Plateau. *Earth Planet. Sci. Lett.* 487, 179–189.

Ifi, Y., Lifu, M., Li, Y., Chen, L., 2019. Active crustal deformation in southeastern Tibetan Plateau: the kinematics and dynamics. *Earth Planet. Sci. Lett.* 523 <https://doi.org/10.1016/j.epsl.2019.07.010>.

Ifi, Y., Shui, F., Zhang, H., Wei, W., Xu, J., Shao, Z., 2020. Coulomb stress change on active faults in Sichuan-Yunnan region and its implications for seismic hazard. *Seismol. Geol.* 42 (2), 526–545.

Ifi, Y., Hao, M., Song, S., Zhu, L., Cui, D., Zhuang, W., Yang, F., Wang, Q., 2021. Interseismic fault slip deficit and coupling distributions on the Annfinghe-Zemuhe-Dafliangshan-Xiaojiaogang fault zone, southeastern Tibetan Plateau, based on GPS measurements. *J. Asian Earth Sci.* 219 <https://doi.org/10.1016/j.jseaes.2021.104899>.

Liu, M., Luo, G., Wang, H., 2014. The 2013 Lushan earthquake in China tests hazard assessments. *Seismol. Res. Lett.* 85 (1), 40–43. <https://doi.org/10.1785/0220130117>.

Luo, G., Lifu, M., 2018. Stressing rates and seismicity on the major faults in eastern Tibetan Plateau. *J. Geophys. Res. Solid Earth*. <https://doi.org/10.1029/2018jb015532>.

Mafervisbi, R., Gans, C., Furong, K.P., 2003. Numerical modeling of strike-slip creeping faults and implications for the Hayward fault, California. *Tectonophysics* 361 (1–2), 121–137. [https://doi.org/10.1016/S0040-1951\(02\)00587-5](https://doi.org/10.1016/S0040-1951(02)00587-5).

Mazzotti, S., Leonard, L.J., Cassidy, J.R., Rogers, G.C., Haschuk, S., 2011. Seismic hazard in western Canada from GPS strain rates versus earthquake catalog. *J. Geophys. Res.* 116 (B12) <https://doi.org/10.1029/2011jb008213>.

Meade, B.J., 2002. Estimates of seismic potential in the Marmara sea region from block models of secular deformation constrained by global positioning system measurements. *Bull. Seismol. Soc. Am.* 92 (1), 208–215. <https://doi.org/10.1785/0120000837>.

Meade, B.J., 2007. Present-day kinematics at the India-Asia collision zone. *Geology* 35 (1), 81–84.

Meade, B.J., Hager, B.H., 2005. Spatial localization of moment deficits in southern California. *J. Geophys. Res. Solid Earth* 110 (B4). <https://doi.org/10.1029/2004jb003331>.

Mfin, Z., Wu, G., Jifang, Z., Lifu, C., Yang, Y., 1995. The Catalogue of Chinese Historical Strong Earthquakes (B.C. 2300–A.D. 1911). Seismological Publishing House, Beijing, China (in Chinese).

Ojo, A.O., Kao, H., Jifang, Y., Craymer, M., Henton, J., 2021. Strain accumulation and release rate in Canada: implications for long-term crustal deformation and earthquake hazards. *J. Geophys. Res. Solid Earth* 126 (4). <https://doi.org/10.1029/2020jb020529>.

Pafano, M., Imprescipe, P., Agnon, A., Gresta, S., 2018. An improved evaluation of the seismic/geodetic deformation-rate ratio for the Zagros fold-and-thrust collisional belt. *Geophys. J. Int.* 213 (1), 194–209. <https://doi.org/10.1093/gji/ggx524>.

Qiao, X., Zhou, Y., 2021. Geodetic imaging of shallow creep along the Xianshuihe fault and its frictional properties. *Earth Planet. Sci. Lett.* 567 <https://doi.org/10.1016/j.epsl.2021.117001>.

Ran, Y.K., Chen, L.C., Cheng, J.W., Gong, H.L., 2008. Late Quaternary surface deformation and rupture behavior of strong earthquake on the segment north of Mianling of the Annfinghe fault. *Sci. China Ser. D Earth Sci.* 51 (9), 1224–1237. <https://doi.org/10.1007/s11430-008-0104-6>.

Reid, H.F., 1910. The California Earthquake of April 18, 1906. Volume II. The Mechanics of the Earthquake. Carnegie Institution of Washington, Washington, D. C.

Shan, B., Xiong, X., Wang, R., Zheng, Y., Yang, S., 2013. Coulomb stress evolution along Xianshuihe-Xiaojiaogang fault system since 1713 and its interaction with Wenchuan earthquake, May 12, 2008. *Earth Planet. Sci. Lett.* 377–378, 199–210. <https://doi.org/10.1016/j.epsl.2013.06.044>.

Shen, Z.K., Lu, J.N., Wang, M., Burgmann, R., 2005. Contemporary crustal deformation around the southeast borderland of the Tibetan Plateau. *J. Geophys. Res. Solid Earth* 110 (B11). <https://doi.org/10.1029/2004jb003421>.

Shen, Z.K., Wang, M., Zeng, Y., Wang, F., 2015. Optimal interpolation of spatially discrete geodetic data. *Bull. Seismol. Soc. Am.* 105 (4), 2117–2127. <https://doi.org/10.1785/0120140247>.

Shi, Y., Boft, B.A., 1982. The standard error of the magnitude-frequency b-value. *Bull. Seismol. Soc. Am.* 72, 1677–1687.

Song, F., Ifi, R., Xu, X., 2002. Preliminary results of the investigation of paleo-earthquakes along the Dafliangshan fault zone, Sichuan province, China. *Seismol. Geol.* 24 (1), 27–34.

Sparacino, F., Paolano, M., Peña, J.A., Fernández, J., 2020. Geodetic deformation versus seismic crustal rate-tectonics: insights from the Ibero-Maghrebian region. *Remote Sens.* 12 (6) <https://doi.org/10.3390/rs12060952>.

Sun, Y., Luo, G., Yfin, L., Shui, Y., 2019. Migration probability of big earthquakes and segmentation of slip rates on the fault system in northeastern Tibetan Plateau. *Chin. J. Geophys. Chin. Ed.* 62 (5), 1663–1679.

Tape, C., Muse, P., Simons, M., Dong, D., Webb, F., 2009. Multi-scale estimation of GPS velocity fields. *Geophys. J. Int.* 179 (2), 945–971. <https://doi.org/10.1111/j.1365-246X.2009.04337.x>.

Tapponnier, P., Xu, Z.Q., Roger, F., Meyer, B., Arnaud, N., Wifflinger, G., Yang, J.S., 2001. Oblique stepwise rise and growth of the Tibetan plateau. *Science* 294 (5547), 1671–1677. <https://doi.org/10.1126/science.105978>.

Wang, M., Shen, Z.K., 2020. Present-day crustal deformation of continental China derived from GPS and its tectonic implications. *J. Geophys. Res. Solid Earth* 125 (2). <https://doi.org/10.1029/2019jb018774>.

Wang, S., Wu, G., Shui, Z., 1999. The Catalogue of Recent Earthquakes in China (A.D. 1912–A.D. 1990). China Science and Technology Publishing House, Beijing, China (in Chinese).

Wang, Y.Z., et al., 2008. GPS-constrained inversion of present-day slip rates along major faults of the Sichuan-Yunnan region, China. *Sci. China Ser. D Earth Sci.* 51 (9), 1267–1283. <https://doi.org/10.1007/s11430-008-0106-4>.

Wang, H., Lifu, M., Shen, X., Lifu, J., 2010. Balance of seismic moment in the Songpan-Ganzi region, eastern Tibet: implications for the 2008 Great Wenchuan earthquake. *Tectonophysics* 491 (1–4), 154–164. <https://doi.org/10.1016/j.tecto.2009.09.022>.

Wang, H., Lifu, M., Cao, J., Shen, X., Zhang, G., 2011. Slip rates and seismic moment deficits on major active faults in mainland China. *J. Geophys. Res. Solid Earth* 116. <https://doi.org/10.1029/2010jb007821>.

Wang, H., Ran, Y., Ifi, Y., Gomez, F., Chen, L., 2014. A 3400-year-long paleoseismological record of earthquakes on the southern segment of Annfinghe fault on the southeastern margin of the Tibetan Plateau. *Tectonophysics* 628, 206–217. <https://doi.org/10.1016/j.tecto.2014.04.040>.

Wang, W., Qiao, X., Yang, S., Wang, D., 2017. Present-day velocity field and block kinematics of Tibetan Plateau from GPS measurements. *Geophys. J. Int.* 208 (2), 1088–1102.

Wang, H., Lifu, M., Duan, B., Cao, J., 2020. Rupture propagation along stepovers of strike-slip faults: effects of initial stress and fault geometry. *Bull. Seismol. Soc. Am.* 110 (3), 1011–1024.

Ward, S., 1998. On the consistency of earthquake moment rates, geologic fault data, and space geodetic strain: the United States. *Geophys. J. Int.* 134 (1), 172–186. <https://doi.org/10.1046/j.1365-246x.1998.00556.x>.

Wefichert, D.H., 1980. Estimation of the earthquake recurrence parameters from unequal observation periods for different magnitudes. *Bull. Seismol. Soc. Am.* 70 (4), 1337–1346.

Wells, D.L., Coppersmith, K.J., 1994. New empirical relationships among magnitude, rupture length, rupture width, rupture area, and surface displacement. *Bull. Seismol. Soc. Am.* 84 (4), 974–1002.

Wen, X.-Z., 2000. Character of rupture segmentation of the Xianshuihe-Annfinghe-Zemuhe fault zone, western Sichuan. *Seismol. Geol.* 22 (3), 239–249 (in Chinese with English abstract).

Wen, X.-Z., Ma, S.-L., Xu, X.-W., He, Y.-N., 2008. Historical pattern and behavior of earthquake ruptures along the eastern boundary of the Sichuan-Yunnan faulted-block, southwestern China. *Phys. Earth Planet. Inter.* 168 (1–2), 16–36. <https://doi.org/10.1016/j.pepi.2008.04.013>.

Wesse, P., Lufis, J.F., Uieda, L., Scharroo, R., Wobbe, F., Smeth, W.H.F., Tsi, D., 2019. The Generic Mapping Tools Version 6. *Geochem. Geophys. Geosyst.* 20 (11), 5556–5564. <https://doi.org/10.1029/2019gc008515>.

Wesson, R.L., 1988. Dynamics of fault creep. *J. Geophys. Res.* 93 (B8), 8929–8951. <https://doi.org/10.1029/JB093fiB08p08929>.

Wiemer, S., 2001. A Software Package to Analyze Seismicity: ZMAP.

Xu, X.W., Wen, X.Z., Zheng, R.Z., Ma, W.T., Song, F.M., Yu, G.H., 2003. Pattern of latest tectonic motion and its dynamics for active blocks in Sichuan-Yunnan region, China. *Sci. China Ser. D Earth Sci.* 46, 210–226. <https://doi.org/10.1360/03d00017>.

Yan, B., Toda, S., Lifu, A., 2018. Coulomb stress evolution history as implication on the pattern of strong earthquakes along the Xianshuihe-Xiaojiaogang fault system, China. *J. Earth Sci.* 29 (2), 427–440. <https://doi.org/10.1007/s12583-018-0840-2>.

Yang, Z.X., Wadhauser, F., Chen, Y.T., Richards, P.G., 2005. Double-difference relocation of earthquakes in Central-Western China, 1992–1999. *J. Seismol.* 9 (2), 241–264. <https://doi.org/10.1007/s10950-005-3988-z>.

Yi, G., Long, F., Wen, X., Lifang, M., Wang, S., 2015. Seismogenic structure of the M 6.3 Kangding earthquake sequence on 22 Nov. 2014, Southwestern China. *Chin. J. Geophys. Chin. Ed.* 58 (4), 1205–1219.

Yfin, L., Luo, G., 2021. Fault interaction and active crustal extrusion in the southeastern Tibetan Plateau: insights from geodynamic modeling. *J. Asian Earth Sci.* 218 <https://doi.org/10.1016/j.jseaes.2021.104866>.

Zhang, P.-Z., 2013. A review on active tectonics and deep crustal processes of the Western Sichuan region, eastern margin of the Tibetan Plateau. *Tectonophysics* 584, 7–22.

Zhang, J., Wen, X.Z., Cao, J.L., Yan, W., Yang, Y.L., Su, Q., 2018. Surface creep and slip behavior segmentation along the northwestern Xianshuihe fault zone of southwestern China determined from decades of fault-crossing short-baseline and short-level surveys. *Tectonophysics* 722, 356–372. <https://doi.org/10.1016/j.tecto.2017.11.002>.

Zhao, G., Meng, G., Wu, W., Su, X., Pan, Z., 2021. Earthquake potential assessment around the Southeastern Tibetan Plateau based on seismic and geodetic data. *Pure Appl. Geophys.* <https://doi.org/10.1007/s00024-021-02917-6>.

Zheng, G., Wang, H., Wright, T.J., Lou, Y.D., Zhang, R., Zhang, W.X., Shi, C., Huang, J.F., Wei, N., 2017. Crustal deformation in the India-Eurasia collision zone from 25 Years of GPS measurements. *J. Geophys. Res. Solid Earth* 122 (11), 9290–9312. <https://doi.org/10.1002/2017jb014465>.

Zhou, R., Ili, X., Huang, Z., He, Y., Ge, T., 2003. Average slip rate of Daliang mountain fault zone in Sichuan in late Quaternary period. *J. Seismol. Res.* 26 (2), 191–196.